

We are IntechOpen, the world's leading publisher of Open Access books Built by scientists, for scientists

6,900

Open access books available

186,000

International authors and editors

200M

Downloads

Our authors are among the

154

Countries delivered to

TOP 1%

most cited scientists

12.2%

Contributors from top 500 universities



WEB OF SCIENCE™

Selection of our books indexed in the Book Citation Index
in Web of Science™ Core Collection (BKCI)

Interested in publishing with us?
Contact book.department@intechopen.com

Numbers displayed above are based on latest data collected.
For more information visit www.intechopen.com



Accurate Modelling of an Injector for Common Rail Systems

Claudio Dongiovanni
*Politecnico di Torino, Dipartimento di Energetica,
Corso Duca degli Abruzzi 24, 10129, Torino
Italy*

Marco Coppo
*O.M.T. S.p.A., Via Ferrero 67/A, 10090, Cascine Vica Rivoli
Italy*

1. Introduction

It is well known that the injection system plays a leading role in achieving high diesel engine performance; the introduction of the common rail fuel injection system (Boehner & Kumel, 1997; Schommers et al., 2000; Stumpp & Ricco, 1996) represented a major evolutionary step that allowed the diesel engine to reach high efficiency and low emissions in a wide range of load conditions.

Many experimental works show the positive effects of splitting the injection process in several pilot, main and post injections on the reduction of noise, soot and NO_x emission (Badami et al., 2002; Brusca et al., 2002; Henelin et al., 2002; Park et al., 2004; Schmid et al., 2002). In addition, the success of engine downsizing (Beatrice et al., 2003) and homogeneous charge combustion engines (HCCI) (Canakci & Reitz, 2004; Yamane & Shimamoto, 2002) is deeply connected with the injection system performance and injection strategy.

However, the development of a high performance common rail injection system requires a considerable investment in terms of time, as well as money, due to the need of fine tuning the operation of its components and, in particular, of the electronic fuel injector. In this light, numerical simulation models represent a crucial tool for reducing the amount of experiments needed to reach the final product configuration.

Many common-rail injector models are reported in the literature. (Amoia et al., 1997; Bianchi et al., 2000; Brusca et al., 2002; Catalano et al., 2002; Ficarella et al., 1999; Payri et al., 2004). One of the older common-rail injector model was presented in (Amoia et al., 1997) and successively improved and employed for the analysis of the instability phenomena due to the control valve behaviour (Ficarella et al., 1999). An important input parameter in this model was the magnetic attraction force in the control valve dynamic model. This was calculated interpolating the experimental curve between driving current and magnetic force measured at fixed control valve positions. The discharge coefficient of the feeding and discharge control volume holes were determined and the authors asserted that the discharge hole operates, with the exception of short transients, under cavitating flow conditions at every working pressure,

but this was not confirmed by (Coppo & Dongiovanni, 2007). Furthermore, the deformation of the stressed injector mechanical components was not taken into account. In (Bianchi et al., 2000) the electromagnetic attraction force was evaluated by means of a phenomenological model. The force was considered directly proportional to the square of the magnetic flux and the proportionality constant was experimentally determined under stationary conditions. The elastic deformation of the moving injector components were considered, but the injector body was treated as a rigid body. The models in (Brusca et al., 2002; Catalano et al., 2002) were very simple models. The aims in (Catalano et al., 2002) were to prove that pressure drops in an injection system are mainly caused by dynamic effects rather than friction losses and to analyse new common-rail injection system configurations in which the wave propagation phenomenon was used to increase the injection pressure. The model in (Brusca et al., 2002) was developed in the AMESim environment and its goal was to give the boundary conditions to a 3D-CFD code for spray simulation. Payri et al. (2004) report a model developed in the AMESim environment too, and suggest silicone moulds as an interesting tool for characterising valve and nozzle hole geometry.

A common-rail injector model employs three sub-models (electrical, hydraulic and mechanical) to describe all the phenomena that govern injector operation. Before one can use the model to estimate the effects of little adjustments or little geometrical modifications on the system performance, it is fundamental to validate the predictions of all the sub-models in the whole range of possible working conditions.

In the following sections of this chapter every sub-model will be thoroughly presented and it will be shown how its parameters can be evaluated by means of theoretical or experimental analysis. The focus will be placed on the electronic injector, as this component is the heart of any common rail system

2. Mathematical model

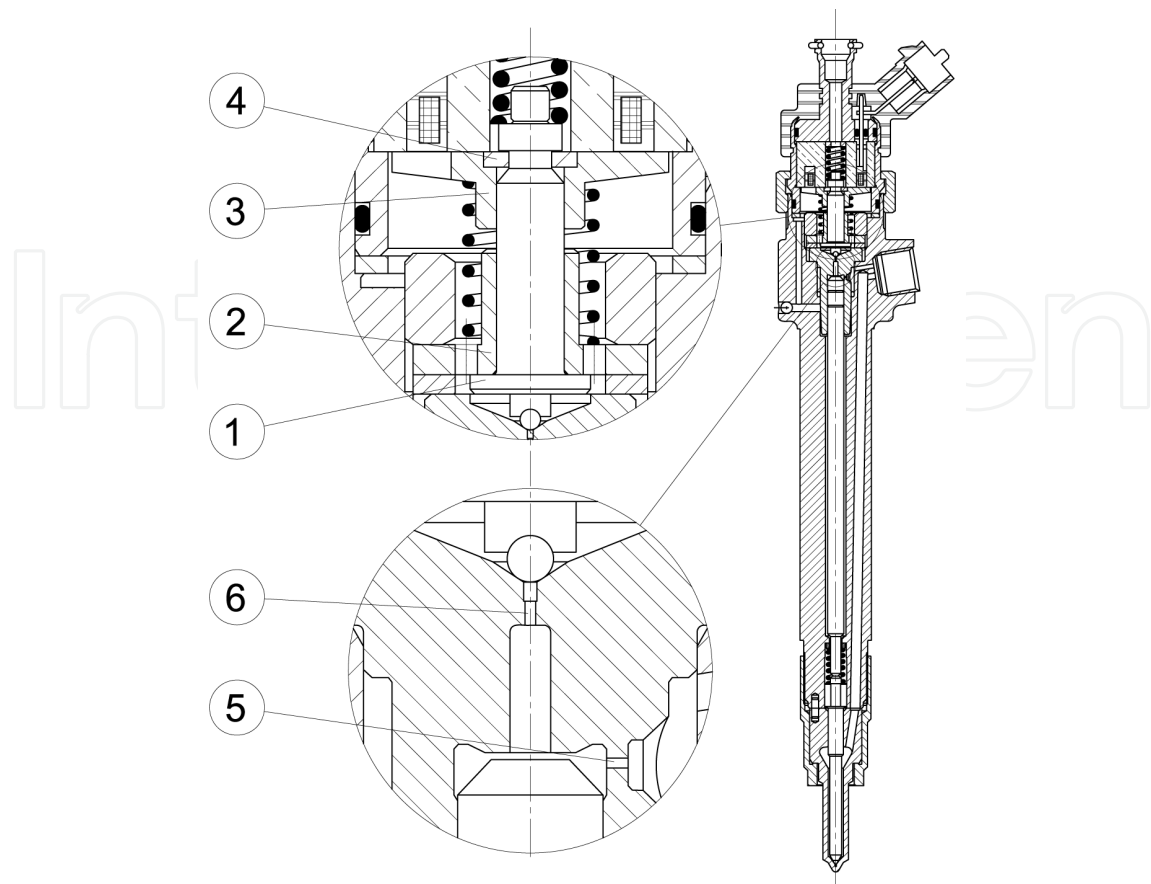
The injector considered in this investigation is a standard Bosch UNIJET unit (Fig. 1) of the common-rail type used in car engines, but the study methodology that will be discussed can be easily adapted to injectors manufactured by other companies.

The definition of a mathematical model always begins with a thorough analysis of the parts that make up the component to be modelled. Once geometrical details and functional relationships between parts are acquired and understood they can be described in terms of mathematical relationships. For the injector, this leads to the definition of hydraulic, mechanical, and electromagnetic models.

2.1 Hydraulic Model

Fig. 2 shows the equivalent hydraulic circuit of the injector, drawn following ISO 1219 standards. Continuous lines represent the main connecting ducts, while dashed lines represent pilot and vent connections. The hydraulic parts of the injector that have limited spatial extension are modelled with ideal components such as uniform pressure chambers and laminar or turbulent hydraulic resistances, according to a zero-dimensional approach. The internal hole connecting injector inlet with the nozzle delivery chamber (as well as the pipe connecting the injector to the rail or the rail to the high pressure pump) are modelled according to a one-dimensional approach because wave propagation phenomena in these parts play an important role in determining injector performance.

Fig. 3a shows the control valve and the relative equivalent hydraulic circuit. R_A and R_Z are the hydraulic resistances used for modelling flow through control-volume orifices A (dis-



| | |
|-----------------------------|---------------------------------------|
| 1. Control valve pin | 4. C-shaped connecting pin and anchor |
| 2. Pin guide and upper stop | 5. Control volume feeding (Z) hole |
| 3. Control valve anchor | 6. Control volume discharge (A) hole |

Fig. 1. Standard Bosch UNIJET injector

charge) and Z (feeding), respectively. The variable resistance R_{AZ} models the flow between chambers C_{dZ} and C_{uA} , taking into account the effect of the control piston position on the actual flow area between the aforementioned chambers. The solenoid control valve V_c is represented using its standard symbol, which shows the forces that act in the opening (one generated by the current I flowing through the solenoid, the other by the pressure in the chamber C_{dA}) and closing direction (spring force).

Fig. 3b illustrates the control piston and nozzle along with the relative equivalent hydraulic circuit. The needle valve V_n is represented with all the actions governing the needle motion, such as pressures acting on different surface areas, force applied by the control piston and spring force. The chamber C_D models the nozzle delivery volume, C_S is the sac volume, whereas the hydraulic resistance R_{hi} represents the i -th nozzle hole through which fuel is injected in the combustion chamber C_e . The control piston model considers two different surface areas on one side, so as to take into account the different contribution of pressure in the chambers C_{uA} and C_{dZ} to the total force applied in the needle valve closing direction.

Leakages both between control valve and piston and between needle and its liner are modelled by means of the resistances R_p and R_n respectively, and the resulting flow, which is collected in chamber C_T (the annular chamber around the control piston), is then returned to

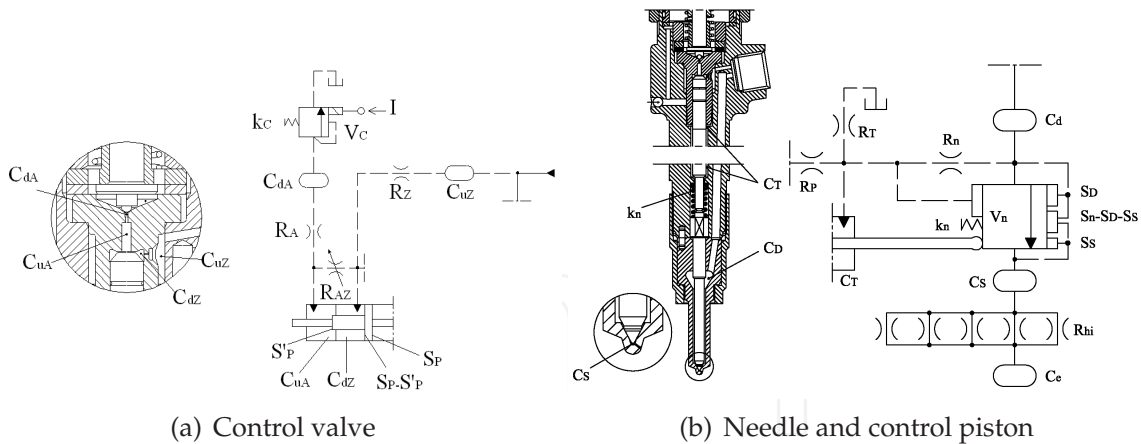


Fig. 3. Injection equivalent hydraulic circuit

Furthermore, the leakage flow rate, Equations 2 and 3, depends on the third power of the radial gap g . At high pressure the material deformation strongly affects the gap entity and its value is not constant along the gap length l because pressure decreases in the gap when approaching the low pressure side (Ganser, 2000). In order to take into account these effects on the leakage flow rate, the value of K_L has to be experimentally evaluated in the real injector working conditions.

Turbulent flow is assumed to occur in control volume feeding and discharge holes, in nozzle holes and in the needle-seat opening passage. As a result, according to Bernoulli's law, the flow rate through these orifices is proportional to the square root of the pressure drop, Δp , across the orifice, namely,

$$Q = \mu A \sqrt{\frac{2\Delta p}{\rho}} \quad (4)$$

The flow model through these orifices plays a fundamental role in the simulation of the injector behavior in its whole operation field, so the evaluation of the μ factor is extremely important.

2.1.2 Hole A and Z discharge coefficient

The discharge coefficient of control volume orifices A and Z is evaluated according to the model proposed in (Von Kuensberg Sarre et al., 1999). This considers four flow regimes inside the hole: laminar, turbulent, reattaching and fully cavitating.

Neglecting cavitation occurrence, a preliminary estimation of the hole discharge coefficient can be obtained as follows

$$\frac{1}{\mu} = \sqrt{K_I + f \frac{l}{d} + 1} \quad (5)$$

where K_I is the inlet loss coefficient, which is a function of the hole inlet geometry (Munson et al., 1990), l is the hole axial length, d is the hole diameter, and f is the wall friction coefficient, evaluated as

$$f = \text{MAX} \left(\frac{64}{Re}, 0.316 Re^{0.25} \right) \quad (6)$$

where Re stands for the Reynolds number.

The ratio between the cross section area of the vena contracta and the geometrical hole area, μ_{vc} , can be evaluated with the relation:

$$\frac{1}{\mu_{vc}^2} = \frac{1}{\mu_{vc0}^2} - 11.4 \frac{r}{d} \quad (7)$$

where $\mu_{vc0} = 0.61$ (Munson et al., 1990) and r is the fillet radius of the hole inlet.

It follows that the pressure in the vena contracta can be estimated as

$$p_{vc} = p_u - \frac{\rho_l}{2} \left(\frac{Q}{A\mu_{vc}} \right)^2 \quad (8)$$

If the pressure in the vena contracta (p_{vc}) is higher than the oil vapor pressure (p_v), cavitation does not occur and the value of the hole discharge coefficient is given by Equation 5. Otherwise, cavitation occurs and the discharge coefficient is evaluated according to

$$\mu = \mu_{vc} \sqrt{\frac{p_u - p_v}{p_u - p_d}} \quad (9)$$

The geometrical profile of the hole inlet plays a crucial role in determining, or avoiding, the onset of cavitation in the flow. In turn, the occurrence of cavitation strongly affects the flow rate through the orifice, as can be seen in Figure 4, which shows two trends of predicted flow rate (Q/Q_0) in function of pressure drop ($\Delta p = p_u - p_d$) through holes with the same diameter and length, but characterized by two different values of the r/d ratio (0.2 and 0.02), when p_u is kept constant and p_d is progressively decreased. In absence of cavitation, ($r/d = 0.2$), the relation between flow rate and pressure drop is monotonic while, if cavitation occurs ($r/d = 0.02$), the hole experiences a decrease in flow rate as pressure drop is further increased. This behavior agrees with experimental data reported in the literature (Lefebvre, 1989).

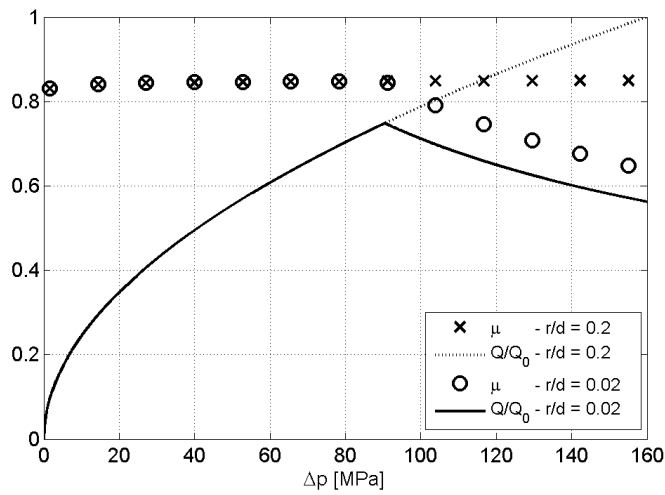


Fig. 4. Predicted flow through an orifice in presence/absence of cavitation

Obviously, such behavior would reflect strongly on the injector performance if the control volume holes happened to cavitate in some working conditions. Therefore, in order to accurately

model the injector operation, it is necessary to accurately measure the geometrical profile of the control volume holes A and Z; by means of silicone moulds, as proposed by (Payri et al., 2004), it is possible to acquire an image of the hole shape details, as shown in Figure 5.

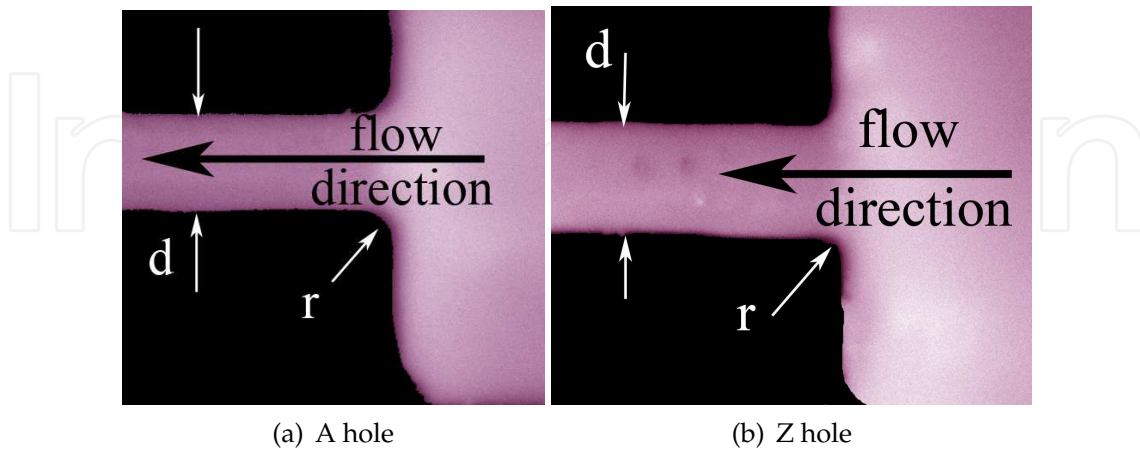


Fig. 5. Moulds of the control valve holes

By means of imaging techniques it is possible to measure the r/d ratio of the hole under investigation. Table 1 reports the results obtained for the injector under investigation. The value of K_I , in Equation 5, is a function of r/d only (Von Kuensberg Sarre et al., 1999) and, hence, easily obtainable.

Knowing that during production a hydro-erosion process is applied to make sure that, under steady flow conditions, all the holes yield the same flow rate, it is possible to define an iterative procedure to calculate the hole diameter using the discharge coefficient model presented above and the steady flow rate value. This approach is preferable to the estimation of the hole diameter with imaging techniques because it yields a result that is consistent with the discharge coefficient model used.

| | r/d | K_I | d [μm] |
|--------|----------------|-------|-----------------------|
| Hole A | $0.23 \pm 5\%$ | 0.033 | $280 \pm 2\%$ |
| Hole Z | $0.22 \pm 5\%$ | 0.034 | $249 \pm 2\%$ |

Table 1. Characteristics of control volume holes

In the control valve used in our experiments, under a pressure drop of 10 MPa, with a back pressure of 4 MPa, the holes A and Z yielded $6.5 \pm 0.2 \text{ cm}^3/\text{s}$ and $5.3 \pm 0.2 \text{ cm}^3/\text{s}$, respectively. With these values it is possible to calculate the most probable diameter of the control volume holes, as reported in Table 1. It is worth noting that the precision with which the diameters were evaluated was higher than that of the optical technique used for evaluating the shape of the control volume holes. This resulted from the fact that K_I shows little dependence on r/d when the latter assumes values as high as those measured. As a consequence, the experimental uncertainty in the diameter estimation is mainly originated from the uncertainty given on the stationary flow rate through the orifices.

2.1.3 Discharge coefficient of the nozzle holes

The model of the discharge coefficient of the nozzle holes is designed on the base of the unsteady coefficients reported in (Catania et al., 1994; 1997). These coefficients were experimentally evaluated for minisac and VCO nozzles in the real working conditions of a distributor pump-valve-pipe-injector type injection system. The pattern of this coefficient versus needle lift evidences three different phases. In the first phase, during injector opening, the moving needle tip strongly influences the efflux through the nozzle holes. In this phase, the discharge coefficient progressively increases with the needle lift. In the second phase, when the needle is at its maximum stroke, the discharge coefficient increases in time, independently from the pressure level at the injector inlet. In the last phase, during the needle closing stroke, the discharge coefficient remains almost constant. These three phases above mentioned describe a hysteresis-like phenomenon. In order to build a model suitable for a common rail injector in its whole operation field these three phases need to be considered.

Therefore, the nozzle hole discharge coefficient is modeled as needle lift dependent by considering two limit curves: a lower limit trend (μ_h^d), which models the discharge coefficient in transient efflux conditions, and an upper limit trend (μ_h^s), which represents the steady-state value of the discharge coefficient for a given needle lift. The evolution from transient to stationary values is modeled with a first order system dynamics.

It was experimentally observed (Catania et al., 1994; 1997) that the transient trend presents a first region in which the discharge coefficient increases rapidly with needle lift, following a sinusoidal-like pattern, and a second region, characterized by a linear dependence between discharge coefficient and needle lift. Thus, the following model is adopted:

$$\mu_h^d(\zeta) = \begin{cases} \mu_h^d(\zeta_0) \sin\left(\frac{\pi}{2\zeta_0} \zeta\right) & 0 \leq \zeta < \zeta_0 \\ \frac{\mu_h^d(\zeta_M) - \mu_h^d(\zeta_0)}{\zeta_M - \zeta_0} (\zeta - \zeta_0) + \mu_h^d(\zeta_0) & \zeta \geq \zeta_0 \end{cases} \quad (10)$$

where ζ is the needle-seat relative displacement, and ζ_0 is the transition value of ζ between the sinusoidal and the linear trend.

The use of the variable ζ , rather than the needle lift, x_n , emphasizes the fact that all the mechanical elements subject to fuel pressure, including nozzle and needle, deform, thus the real variable controlling the discharge coefficient is not the position of the needle, but rather the effective clearance between the latter and the nozzle.

The maximum needle lift, ζ_M , varies with rail pressure due to the different level of deformation that this parameter induces on the mechanical components of the injector. The relation between ζ_M and the reference rail pressure p_{r0} is assumed to be linear as

$$\zeta_M = K_1 p_{r0} + K_2 \quad (11)$$

where K_1 and K_2 are constants that are evaluated as explained in the section 2.3.3.

Similarly, the value of ζ_0 in Equation 10 is modeled as a function of the operating pressure p_{r0} in order to better match the experimental behavior of the injection system. Thus, the following fit is used

$$\zeta_0 = K_3 p_{r0} + K_4 \quad (12)$$

and K_3 and K_4 are obtained at the end of the model tuning phase (table 4).

In order to define the relation between the steady state value of the nozzle-hole discharge coefficient (μ_h^s) and the needle-seat relative displacement (ζ) the device in Figure 6 was designed. It contains a camshaft that can impose to the needle a continuously variable lift up to

1 mm. Then, a modified injector equipped with this device was connected to the common rail injection system and installed in a Bosch measuring tube, in order to control the nozzle hole downstream pressure. The steady flow rate was measured by means of a set of graduated burettes.

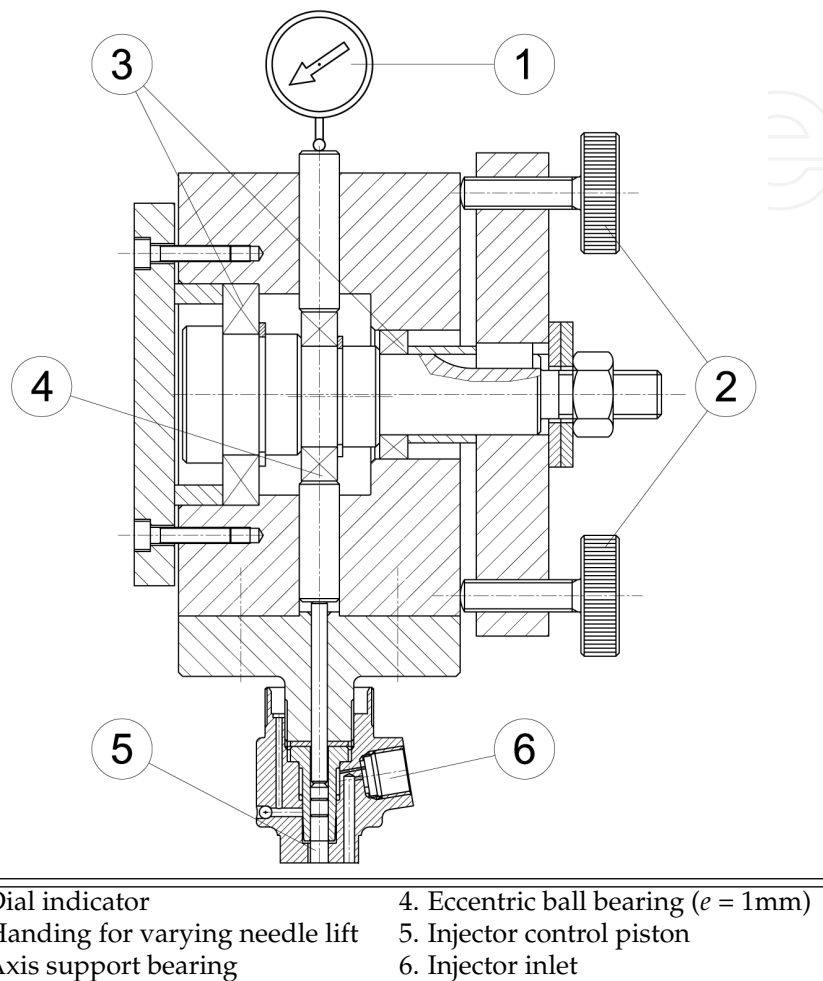


Fig. 6. Device for fixed needle-seat displacement imposition

Figure 7a shows the trends of steady-state flow rate versus needle lift at rail pressures of 10 and 20 MPa, while the back pressure in the Bosch measuring tube was kept to either ambient pressure or 4 MPa; whereas Figure 7b shows the resulting stationary hole discharge coefficient, evaluated for the nozzle under investigation.

Taking advantage of the reduced variation of μ_h^s with operation pressure, it is possible to use the measured values to extrapolate the trends of steady-state discharge coefficient for higher pressures, thus defining the upper boundary of variation of the nozzle hole discharge coefficient values.

During the injector opening phase the unsteady effects are predominant and the sinusoidal-linear trend of the hole discharge coefficient, Equation 10, was considered; when the needle-seat relative displacement approaches its relative maximum value ξ_M^r , the discharge coefficient increases in time, which means that the efflux through the nozzle holes is moving to the stationary conditions. In order to describe this behavior, a transition phase between the

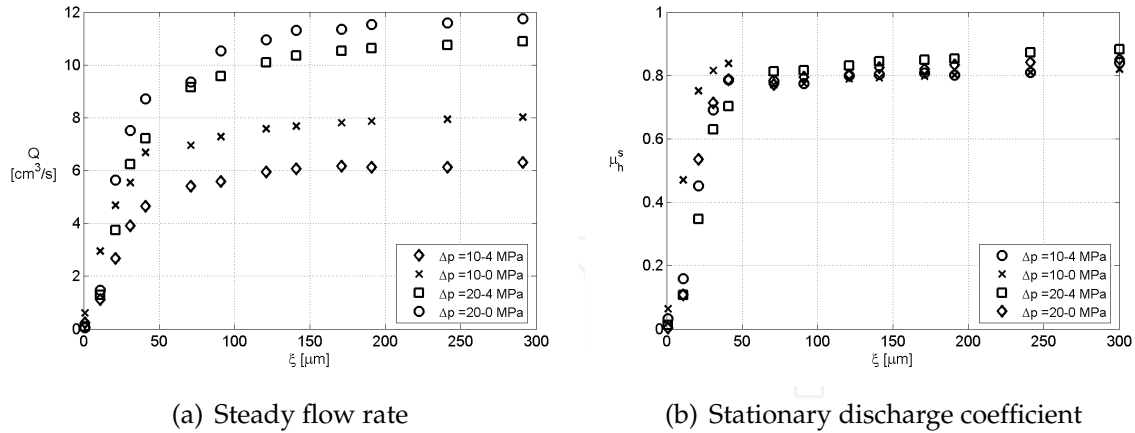


Fig. 7. Stationary efflux through the nozzle

unsteady and the stationary values of the hole discharge coefficient at this needle lift was considered. This phase was modeled as a temporal exponential curve, namely,

$$\mu_h = \mu_h^d(\zeta_M^r) + [\mu_h^s(\zeta_M^r) - \mu_h^d(\zeta_M^r)] [1 - \exp(-\frac{t - t_0}{\tau})] \quad (13)$$

where t_0 is the instant in time at which the needle-seat relative displacement approaches its maximum value ζ_M^r , $\mu_h^d(\zeta_M^r)$ and $\mu_h^s(\zeta_M^r)$ are the unsteady and the stationary hole discharge coefficients evaluated at this needle-seat relative displacement, and τ is the time constant of this phenomenon, which have to be defined during the model tuning phase.

Figure 8 shows the computed nozzle hole discharge coefficient, μ_h , dependence upon needle-seat relative displacement, ζ , in accordance to the proposed model, in a wide range of operating conditions (which are showed by rail pressure p_{r0} and energisation time ET_0 in the legend).

Examining the discharge coefficient, μ_h , trends for the three main injections ($ET_0 = 780 \mu\text{s}$, $700 \mu\text{s}$ and $670 \mu\text{s}$) during the opening phase, it is interesting to note that for a given value of the needle lift, lower discharge coefficients are to be expected at higher operating pressures. This can be explained considering that the flow takes longer to develop if the pressure differential, and thus the steady state velocity to reach is higher.

The main injection trends also show the transition from the sinusoidal to the linear dependence of the transient discharge coefficient on needle lift.

The phase in which the needle has reached the maximum value and the discharge coefficient increases in time from unsteady to stationary values is not very evident in main injections, because the former increases enough during the opening phase to approach the latter. This happens because the needle reaches sufficiently high lifts as to have reduced effect on the flow in the nozzle holes, and the longer injection allows time for complete flow development.

Conversely, during pilot injections ($ET_0 = 300 \mu\text{s}$), the needle reaches lower maximum lifts, hence lower values of the unsteady discharge coefficient, so that the phase of transition to the stationary value lasts longer. The beginning of this transition can be easily identified by analyzing the curves marked with dots and crosses in Figure 8. The point at which they depart from their main injection counterpart (same line style but without markers) marks the beginning of the exponential evolution in time to stationary value of discharge coefficient.

For both pilot and main injections, the nozzle hole discharge coefficient remains constant, and equal to the stationary value, during the injector closing phase, as shown by the horizontal profile of the trends in Figure 8.

The needle-seat discharge coefficient μ_s has to be modeled too. It is assumed as needle lift dependent according to (Xu et al., 1992) where this coefficient was experimentally evaluated after removing the nozzle tip. A three segment trend is considered, as shown in Fig. 8, but it is worth to point out that it plays a marginal role in the injection system simulation because its values are higher than 0.8 for most needle lift values.

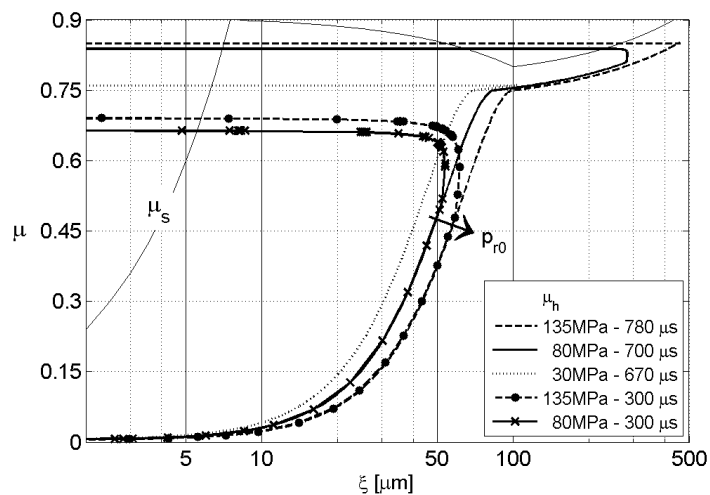


Fig. 8. Needle-seat and holes discharge coefficient

2.1.4 One-dimensional model: pipe flow model

A one-dimensional modelling approach is followed in order to model the fluid flow in the pipe connecting injector and rail and in the injector internal duct that carries the fluid from the inlet to the delivery chamber. This is necessary to correctly take into account pressure wave propagation that occurs in those elements. The pipe flow conservation equations are written for a single-phase fluid because in the common-rail injection system cavitation does not appear in the connecting pipe. An isothermal flow is assumed and only the momentum and mass conservation equations need to be solved

$$\frac{\partial \mathbf{w}}{\partial t} + A \frac{\partial \mathbf{w}}{\partial x} = \mathbf{b} \quad (14)$$

$$\text{where } \mathbf{w} = \begin{Bmatrix} u \\ p \end{Bmatrix}, A = \begin{Bmatrix} u & 1/\rho \\ \rho c^2 & u \end{Bmatrix}, \mathbf{b} = \begin{Bmatrix} -4\tau/\rho d \\ 0 \end{Bmatrix}$$

and τ is the wall shear stress that is evaluated under the assumption of steady-state friction (Streeter et al., 1998).

The eigenvalues of the hyperbolic system of partial differential Equations 14 are $\lambda = u \pm c$, real and distinct. The celerity c of the wave propagation can be evaluated as

$$c = \sqrt{\frac{c_l}{\left(1 + K_p \frac{E_l}{E_p} \frac{d_p}{t_p}\right)}} \quad (15)$$

where the second term within brackets takes into account the effect of the pipe elasticity; K_p is the pipe constraint factor, depending on pipe support layout, E_p the Young's modulus of elasticity of the pipe material, d_p the pipe diameter and t_p the pipe wall thickness (Streeter et al., 1998). Being the pipe ends rigidly constrained, the pipe constrain factor K_p can be evaluated as

$$K_p = 1 - \nu_p^2 \quad (16)$$

where ν_p is the Poisson's modulus of the pipe material.

Pipe junctions are treated as minor losses and only the continuity equation is locally written. As mentioned before, this simple pipe flow model is not suitable when cavitation occurs. This is not a limitation when common-rail injection system are modelled because of the high pressure level at which these systems always work. In order to model conventional injection systems, as pump-pipe-nozzle systems, it is necessary to employ a pipe flow model able to simulate the cavitation occurrence. For this purpose the authors developed an appropriate second order model (Dongiovanni et al., 2003).

2.1.5 Fluid properties

Thermodynamic properties of oil are affected by temperature and pressure that remarkably vary in the common rail injection system operation field. Density, wave propagation speed and kinematic viscosity of the ISO4113 air-free test oil had been evaluated as function of pressure and temperature (Dongiovanni, 1997). These oil properties were approximated with analytic functions of the exponential type in the range of pressures from 0.1 to 200 MPa and temperatures from 10 °C to 120 °C. These analytic relations were derived from the actual property values supplied by the oil maker, by using the least-square method for non-linear approximation functions with two independent variables. The adopted formulae are:

$$\rho_l(p, T) = K_{\rho 1} + \left[1 - \exp\left(-\frac{p}{K_{\rho 2}}\right) \right] K_{\rho 3} p^{K_{\rho 4}} \quad (17)$$

$$E_l(p, T) = K_{E 1} + \left[1 - \exp\left(-\frac{p}{K_{E 2}}\right) \right] K_{E 3} p^{K_{E 4}} \quad (18)$$

$$\nu_l(p, T) = K_{\nu 1} + K_{\nu 2} p^{K_{\nu 3}} \quad (19)$$

The K_{Ei} , $K_{\rho i}$ and $K_{\nu i}$ are polynomial functions of temperature T

$$K_i = \sum_{j=0}^{l_i} K_{i,j} T^j \quad i = 1, 2, 3, 4 \quad (20)$$

and the numerical coefficients that appear in them are reported in Table 2 according with SI units: pressure $[p] = \text{bar}$, temperature $[T] = ^\circ \text{C}$, density $[\rho_l] = \text{kg}/\text{m}^3$, bulk modulus $[E_l] = \text{MPa}$ and kinematic viscosity $[\nu_l] = \text{mm}^2/\text{s}$

Finally, the celerity of the air free oil is evaluate in accordance with $c_l = \sqrt{E_l/\rho_l}$.

By using these approximation functions, the maximum deviation between experimental and analytical values in the examined range of pressure and temperature has been estimated as being lower than $\pm 0.2\%$ for density, $\pm 1.2\%$ for bulk modulus, $\pm 0.6\%$ for celerity and $\pm 18\%$ for kinematic viscosity.

| | | | | |
|----------------|-----------|------------|-----------|------------|
| K_ρ | j= 0 | j= 1 | j= 2 | |
| $K_{\rho 1,j}$ | 8.3636e2 | -6.7753e-1 | - | |
| $K_{\rho 2,j}$ | 1.5063e2 | -2.4202e-1 | - | |
| $K_{\rho 3,j}$ | 1.7784e-1 | 1.4640e-3 | 1.5402e-5 | |
| $K_{\rho 4,j}$ | 7.8109e-1 | -8.1893e-4 | - | |
| K_E | j= 0 | j= 1 | j= 2 | |
| $K_{E1,j}$ | 1.7356e3 | -1.0908e1 | 2.2976e-2 | |
| $K_{E2,j}$ | 7.5540e1 | - | - | |
| $K_{E3,j}$ | 1.5050 | -3.7603e-3 | - | |
| $K_{E4,j}$ | 9.4448e-1 | 3.9441e-4 | - | |
| K_v | j=0 | j=1 | j=2 | j=3 |
| $K_{v1,j}$ | 6.4862 | -1.5847e-1 | 1.6342e-3 | -6.0334e-6 |
| $K_{v2,j}$ | 4.0435e-4 | -2.3118e-6 | - | - |
| $K_{v3,j}$ | 1.4346 | -6.2288e-3 | 3.3500e-5 | - |

Table 2. Polynomial coefficients for ISO4113 oil

2.2 Electromagnetic model

A model of the electromechanical actuator that drives the control valve must be realized in order to work out the net mechanical force applied by the solenoid on its armature, for a given current flowing in the solenoid. The magnetic force applied by the solenoid on the armature F_{Ea} can be obtained by applying the principle of energy conservation to the armature-coil system (Chai, 1998; Nasar, 1995). In the general form it can be written as follows:

$$V I dt = F_{Ea} dx_a + dW_m \quad (21)$$

where $V I dt$ represents the electric energy input to the system, $F_{Ea} dx_a$ is the mechanical work done on the armature and dW_m is the change in the magnetic energy.

From Faraday's law, voltage V may be expressed in terms of flux linkage ($N \frac{d\Phi}{dt}$) and Equation 21 becomes

$$N I d\Phi = F_{Ea} dx_a + dW_m \quad (22)$$

as shown in (Chai, 1998; Nasar, 1995); by considering Φ and x_a as independent variables, Equation 22 can be reduced to

$$F_{Ea} = - \left. \frac{\partial W_m}{\partial x_a} \right|_{\Phi} \quad (23)$$

The magnetic circuit geometry of the control valve needs to be thoroughly analyzed in order to evaluate the magnetic energy stored in the gap. Fig. 9a shows the path of the significant magnetic fluxes, having neglected secondary leakage fluxes and flux fringing.

Exploiting the analogy between Ohm's and Hopkinson's law, it is possible to obtain the magnetic equivalent circuit of Fig. 9b where NI is the ampere-turns in the exciting coil and \mathcal{R}_j ($j = 1, \dots, 5$) are the magnetic reluctances. When the magnetic flux flows across a cross-section area A_a constant along the path length l , the value of the j -th reluctance can be obtained by:

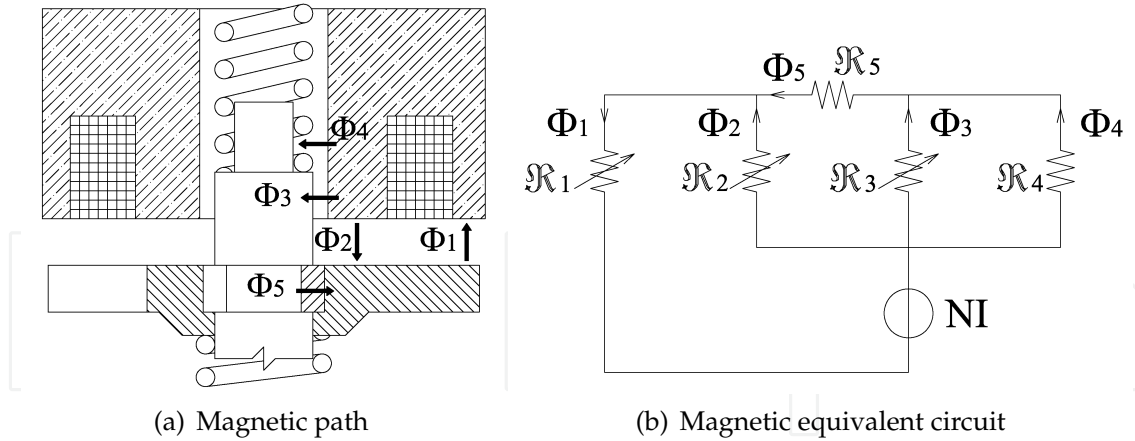


Fig. 9. Magnetic model sketch

$$\mathcal{R}_j = \frac{l_j}{\mu_0 A_{aj}} \quad (j = 1, 2) \quad (24)$$

When the flux flows across a radial path, the reluctance can be evaluated as

$$\mathcal{R}_j = \frac{1}{2\pi\mu_0 t_j} \ln \left(\frac{d_e}{d_i} \right)_j \quad (j = 3, 4, 5) \quad (25)$$

being t the radial thickness, d_e and d_i the external and internal diameter of the gap volume. Reluctance of the ferromagnetic components was neglected because it is several order of magnitude lower than the corresponding gap reluctance.

Circuit of Fig. 9b is solved using Thevenin's theorem, and the equivalent circuit reluctance connected to the magnetomotive force generator is determined as

$$\mathcal{R} = \mathcal{R}_1 + \frac{\mathcal{R}_2 \mathcal{R}_3 \mathcal{R}_4 + \mathcal{R}_2 \mathcal{R}_5 (\mathcal{R}_3 + \mathcal{R}_4)}{\mathcal{R}_3 \mathcal{R}_4 + (\mathcal{R}_2 + \mathcal{R}_5) (\mathcal{R}_3 + \mathcal{R}_4)} \quad (26)$$

The magnetic energy W_m is stored in the volume of the electromechanical actuator, but only the portion of energy stored in the gap between control-valve body and magnetic core depends on the armature lift x_a . Consequently, being the magnetization curve of non-ferromagnetic materials (oil in the gaps) linear, Equation 23 can be written as

$$F_{Ea} = -\frac{1}{2} \Phi^2 \frac{d\mathcal{R}}{dx_a} = -\frac{1}{2} \left(\frac{NI}{\mathcal{R}} \right)^2 \frac{d\mathcal{R}}{dx_a} \quad (27)$$

To complete the model, it was necessary to take into account the saturation phenomenon that occurs to every ferromagnetic material. That is, a magnetic flux cannot increase indefinitely, as the material presents a maximum magnetic flux density after which the curve $B - H$ is almost flat. In this model we assumed a simplified magnetization curve, given by :

$$B = \begin{cases} \mu H & H < H^* \\ \mu H^* + \mu_0 (H - H^*) & H \geq H^* \end{cases} \quad (28)$$

thus neglecting material hysteresis and non-linearity.

As a result of the saturation phenomenon, the maximum force of attraction is limited because the maximum magnetic flux which can be obtained in the j -th branch of the circuit is approximately

$$\Phi_{Mj} \approx \mu H_j^* A_j \quad (29)$$

being μ_0 negligible with respect μ .

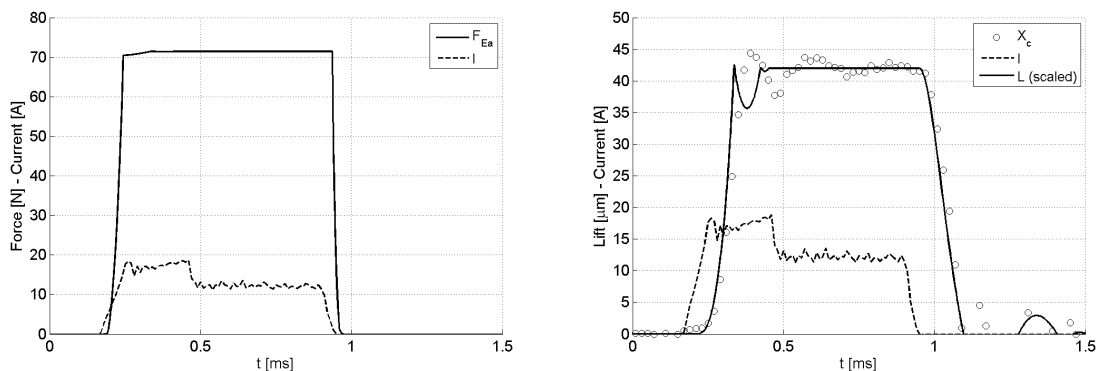
The most important parameters in the electromagnetic model are set as reported in Table 3.

| N | $B^* = \mu H^*$ [T] | t_3 [mm] | t_4 [mm] | t_5 [mm] |
|----|---------------------|------------|------------|------------|
| 32 | 2.5 | 0.65 | 1.5 | 0.05 |

Table 3. Most important electromagnetic model parameters

The model was employed to evaluate the inductance of the solenoid when mounted on the injector body. In this case, with the valve actuator in the closed position, an inductance of $134 \mu H$ was evaluated. Employing a sinusoidal wave generator at a frequency of 5 kHz, which is high enough to make negligible the mechanical system movements, an inductance of $137 \mu H$ was measured. The accordance between experimental and theoretical inductance value indirectly validates the electromagnetic model and the parameters value.

Fig. 10a shows the theoretical (solid line) driving actuator force when the actual energizing current (dashed line) is used to feeding the injector solenoid.



(a) Magnetic force and feeding current

(b) Inductance and armature lift

Fig. 10. Magnetic model results

Furthermore, we point out that the measure of the injector coil inductance $L = N/\mathcal{R}^2$ could be used to indirectly evaluate the control valve lift, due to the dependence of reluctance upon armature distance from the solenoid (Equation 24).

Bearing in mind that, by applying Ohm's law to the solenoid coil, the inductance L could be evaluated as:

$$L = \frac{\int (V - RI) dt}{I} \quad (30)$$

hence only the measurement of solenoid current I and voltage V would be required to calculate L .

Fig. 10b draws the theoretical inductance L , which was calculated according to Equation 24 and opportunely scaled, compared to the experimental valve lift x_c , showing a good agreement between the two trends, and hence the potential of this non-invasive measurement technique. However, Equation 30 is only applicable when electric current is flowing in the solenoid coil so, for example, it is not possible to use this method to record the the control valve closure trend because, as Fig. 10b shows, this usually begins when the solenoid current is null.

A possible way to solve this problem would be to inject an additional, small amplitude, high frequency (around 1 MHz) current into the coil, but this technique has not yet been tested by the authors.

2.3 Mechanical model

All mechanical devices that can move during injector functioning (i.e. needle, control piston and control valve) are modelled using the conventional mass-spring-damper scheme, governed by a mechanical equilibrium equation, in which the dynamic parameters are function of element position.

$$m_j \frac{d^2 x_j}{dt^2} + \bar{\beta}_j \frac{dx_j}{dt} + \bar{k}_j x_j + \bar{F}_{0j} = F_j \quad (31)$$

where m_j is the displacing mass, $\bar{\beta}_j$ the damping coefficient, \bar{k}_j the spring stiffness and \bar{F}_{0j} the spring preload; the bar above the symbols indicates that these coefficients are evaluated according to the relative position of the moving elements.

2.3.1 Control piston, needle and nozzle model

The high working pressures in the common-rail injection system stress its components and cause appreciable deformation of them. In order to take into account the effects of the axial deformation of nozzle and injector body, the nozzle is modelled by means of a conventional mass-spring-damper scheme as well as the needle and the control piston, while the injector body is modelled by means of a simple spring having appropriate stiffness.

Injector needle, control piston and nozzle form a three degrees of freedom mechanical system, which can be modelled as shown in Figure 11a. Three equilibrium equations are needed to describe the system motion, one for each element. With reference to Fig. 11a, the dynamic equilibrium Equation 31 is written using the following definition for the control piston ($j = P$), the needle ($j = n$) and the nozzle ($j = N$):

external force F_j :

$$\begin{aligned} F_P &= -F_c + p_T S_P + F_{R(Pn)} - F_{R(Pb)} \\ F_n &= -p_T S_n - F_{R(Pn)} + F_S + F_{R(nN)} \\ F_N &= -F_S + p_e S_n - F_{R(nN)} \end{aligned} \quad (32)$$

where $F_{R(ij)}$ is the force that i -th and j -th element apply to each other when they are in contact,

$$F_c = p_{uA} S'_P + p_{dZ} (S_P - S'_P) \quad (33)$$

and

$$F_S = p_S S_S + p_D S_D + [\gamma p_S + (1 - \gamma) p_D] (S_n - S_D - S_S) \quad (34)$$

where $\gamma = 0$ indicates that the nozzle is closed while $\gamma = 1$ indicates open nozzle conditions. Damping coefficient $\bar{\beta}_j$, stiffness \bar{k}_j and preload \bar{F}_{0j} are evaluated as follows for: control piston

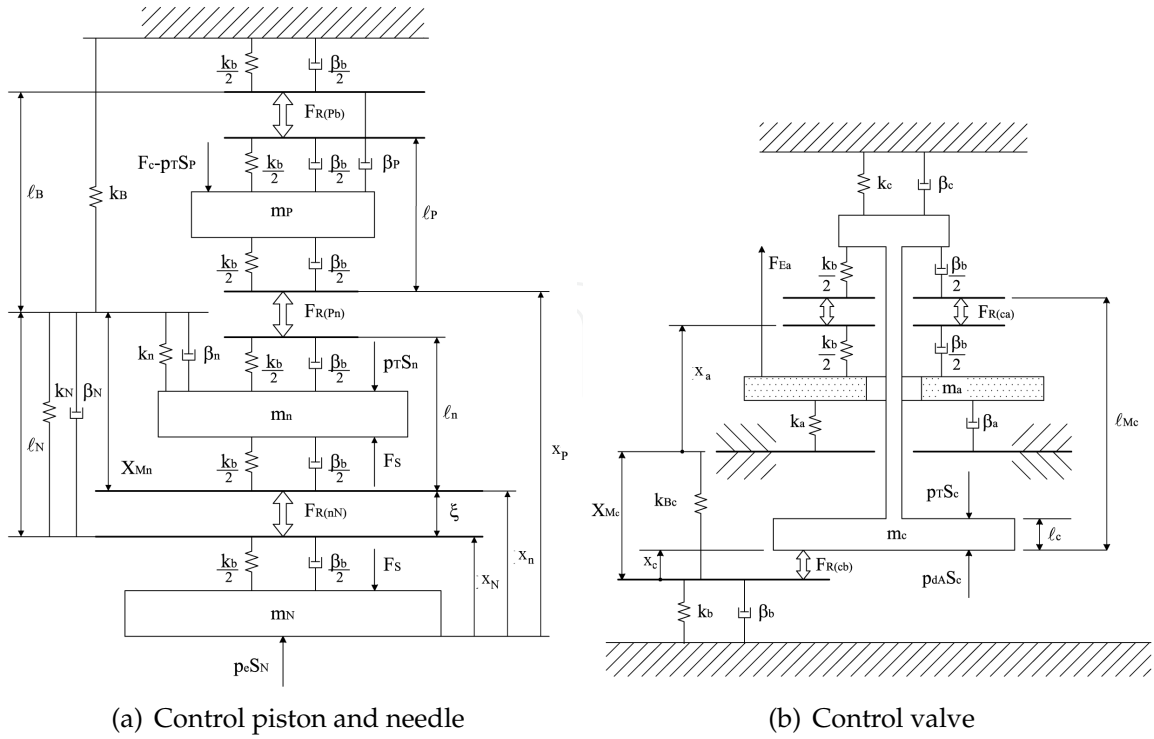


Fig. 11. Dynamic models

$$\begin{aligned}
 x_P < X_{MP} - l_P & \quad \overline{\beta_P} = \beta_P & \quad \overline{k_P} = 0 & \quad \overline{F_{0P}} = 0 \\
 X_{MP} - l_P \leq x_P & \quad \overline{\beta_P} = \beta_b + \beta_P & \quad \overline{k_P} = k_b & \quad \overline{F_{0P}} = -k_b(X_{MP} - l_P)
 \end{aligned} \quad (35)$$

needle

$$\begin{aligned}
 x_n - x_N < 0 & \quad \overline{\beta_n} = \beta_b + \beta_n & \quad \overline{k_n} = k_b + k_n & \quad \overline{F_{0n}} = F_{0n} \\
 0 \leq x_n - x_N < X_{Mn} - l_n & \quad \overline{\beta_n} = \beta_n & \quad \overline{k_n} = k_n & \quad \overline{F_{0n}} = F_{0n} \\
 X_{Mn} - l_n \leq x_n - x_N & \quad \overline{\beta_n} = \beta_b + \beta_n & \quad \overline{k_n} = k_b + k_n & \quad \overline{F_{0n}} = F_{0n} - k_b X_{Mn}
 \end{aligned} \quad (36)$$

nozzle

$$\begin{aligned}
 x_n - x_N < 0 & \quad \overline{\beta_N} = \beta_b + \beta_N & \quad \overline{k_N} = k_b + k_N & \quad \overline{F_{0N}} = 0 \\
 0 \leq x_n - x_N & \quad \overline{\beta_N} = \beta_N & \quad \overline{k_N} = k_N & \quad \overline{F_{0N}} = 0
 \end{aligned} \quad (37)$$

2.3.2 Control valve model

The control valve contains two mobile parts: the pin element having mass m_c and the armature element of mass m_a ; they can be modelled with the two degrees of freedom scheme shown in Fig. 11b. The two dynamic equilibrium equations are written in a similar fashion as Equation 31 where $j = a$ indicates the armature and $j = c$ the control-pin. The external forces F_j can be evaluated as

$$\begin{aligned}
 F_a &= F_{Ea} - F_{R(ca)} \\
 F_c &= (p_{dA} - p_T)S_c + F_{R(ca)} + F_{R(cb)}
 \end{aligned} \quad (38)$$

where F_{Ea} represents the electromagnetic action that the current generates when it flows in the solenoid coil determined as shown in section 2.2.

Damping coefficient $\overline{\beta}_j$, stiffness \overline{k}_j and preload \overline{F}_{0j} are evaluated as follows:
pin element

$$\begin{aligned} x_c < 0 & \quad \overline{\beta}_c = \beta_b + \beta_c & \quad \overline{k}_c = k_b + k_c & \quad \overline{F}_{0c} = F_{0c} \\ 0 \leq x_c < X_{Mc} - l_c & \quad \overline{\beta}_c = \beta_c & \quad \overline{k}_c = k_c & \quad \overline{F}_{0c} = F_{0c} \\ X_{Mc} - l_c \leq x_c & \quad \overline{\beta}_c = \beta_b + \beta_c & \quad \overline{k}_c = k_b + k_c & \quad \overline{F}_{0c} = F_{0c} - k_b(X_{Mc} - l_c) \end{aligned} \quad (39)$$

armature

$$\begin{aligned} l_{Mc} - X_{Mc} + x_c \geq x_a & \quad \overline{\beta}_a = \beta_a & \quad \overline{k}_a = k_a & \quad \overline{F}_{0a} = F_{0a} \\ x_a > l_{Mc} - X_{Mc} + x_c & \quad \overline{\beta}_a = \beta_b + \beta_a & \quad \overline{k}_a = k_b + k_a & \quad \overline{F}_{0a} = F_{0a} - k_b(l_{Mc} - X_{Mc} + x_c) \end{aligned} \quad (40)$$

2.3.3 Mechanical components deformation

The axial deformation of needle, nozzle and control piston have to be taken into account. These elements are considered only axially stressed, while the effects of the radial stress are neglected. For the sake of simplicity, the axial length of control piston (l_p), needle (l_n), and nozzle (l_N) can be evaluated as function of the axial compressive load (F_C) in each element. Therefore, the deformed length l of these elements, which are considered formed by m parts having cross section A_j and initial length l_{0j} , is evaluated as follows

$$l = \sum_j^m l_{0j} \left(1 - \frac{F_{Cj}}{EA_j} \right) \quad (41)$$

where E is Young's modulus of the considered material.

The axial deformation of the injector body is taken into account by introducing in the model the elastic elements indicated as k_B and k_{BC} in Figure 11.

The injector body deformation cannot be theoretically calculated very easily, because one should need to take into account the effect and the deformation of the constraints that fix the injector on the test rig. For this reason, in order to evaluate the elasticity coefficient of k_B and k_{BC} , an empirical approach is followed, which consists in obtaining a relation between the axial length of these elements and the fluid pressure inside the injector body. As direct consequence, the maximum stroke of the needle-control piston (ξ_M) and of the control-valve (X_{Mc}) can be expressed as a function of the injector structural stress.

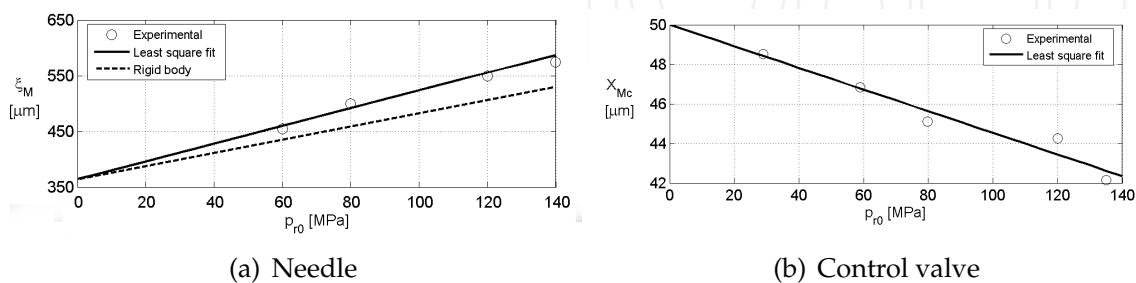


Fig. 12. Effect of pressure on the maximum moving element lift

Figure 12 reports the actual maximum needle-control piston lift (circular symbols) as a function of rail pressure. At the rail pressure of 30 MPa the maximum needle-control piston lift was

not reached, so no value is reported at this rail pressure. The continuous line represents the least-square fit interpolating the experimental data and the dashed line shows the maximum needle-control piston lift calculated by considering only nozzle, needle and control-piston axial deformation. The difference between the two lines represents the effect of the injector body deformation on the maximum needle-control piston lift. This can be expressed as a function of rail pressure and, for the considered injector, can be estimated in $0.41 \mu\text{m}/\text{MPa}$. By means of the linear fit (continuous line) reported in Figure 12 it is possible to evaluate the parameters $K_1 = 1.59 \mu\text{m}/\text{MPa}$ and $K_2 = 364 \mu\text{m}$ that appear in Eq. 11.

In order to evaluate the elasticity coefficient k_{BC} , an analogous procedure can be followed by analyzing the maximum control-valve lift dependence upon fuel pressure, as shown in Figure 12. It was found that the effect of injector body deformation was that of reducing the maximum control valve stroke of $0.06 \mu\text{m}/\text{MPa}$.

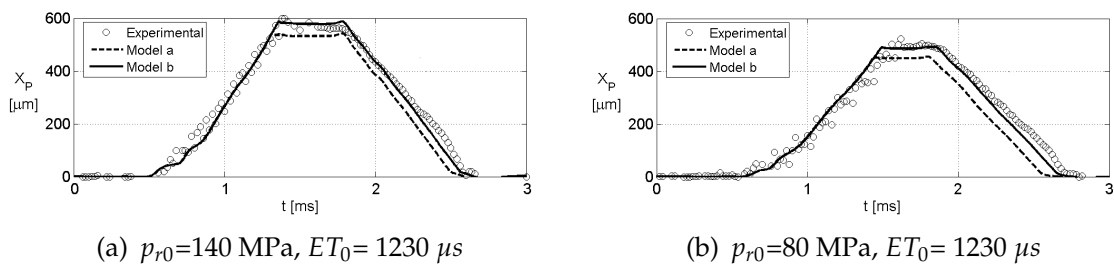


Fig. 13. Deformation effects on needle lift

The relevance of the deformation effects on the injector predicted performances is shown in Fig. 13. The left graph shows the control piston lift at a rail pressure of 140 MPa generated with an energizing time ET_0 of $1230 \mu\text{s}$, while the right graph shows the same trend at a rail pressure of 80 MPa, and generated with the same value of ET_0 . The experimental results are drawn by circular symbols, while lines refer to theoretical results. The dashed lines (Model a) show the theoretical control piston lift evaluated by only taking in to account the axial deformation of the moving elements and nozzle, while the continuous lines (Model b) show the theoretical results evaluated by taking into account the injector body deformation too. The difference between the two models is significant, and so is the underestimation of the volume of fluid injected per stroke (4.3% with $p_{r0}=140 \text{ MPa}$ and ET_0 of $1230 \mu\text{s}$, 3.6% with $p_{r0}=80 \text{ MPa}$, ET_0 of $1230 \mu\text{s}$). This highlights the necessity of accounting for deformation of the entire injector body, if accurate predictions are sought.

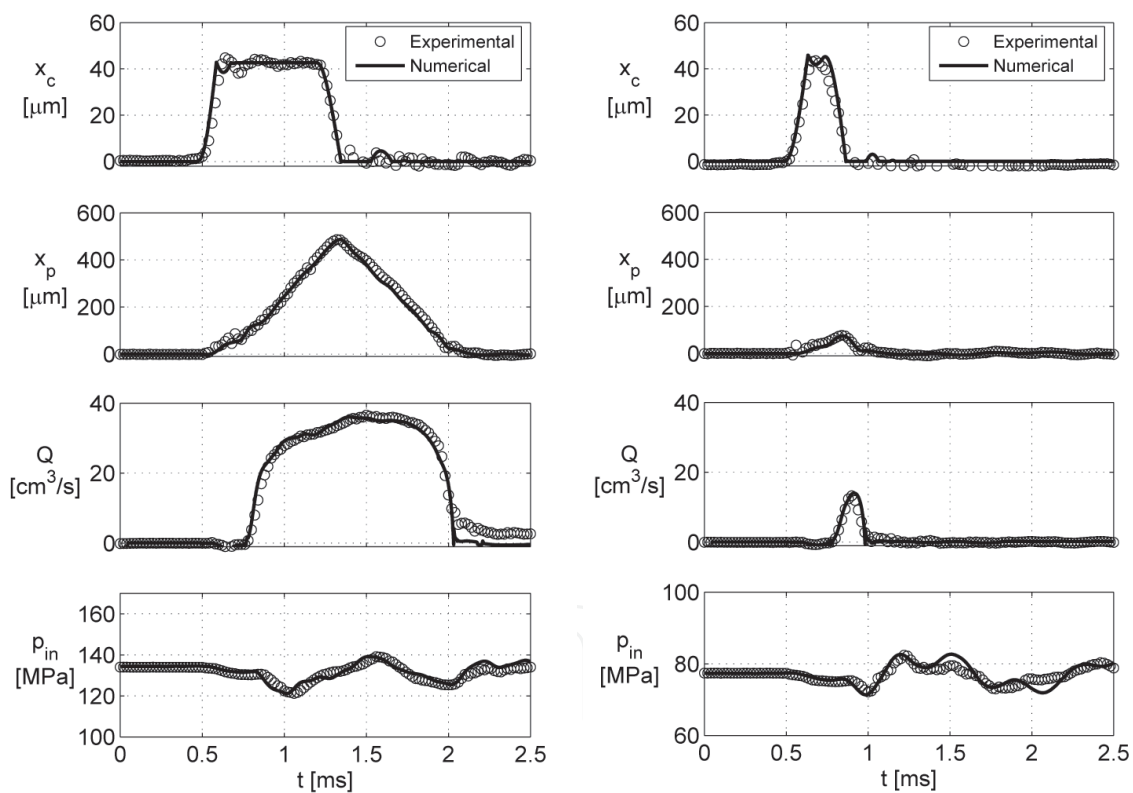
Indeed, the maximum needle lift evaluation plays an important role in the simulation of the injector behaviour in its whole operation field because it influences both the calculation of the injected flow rate (as the discharge coefficients of needle-seat and nozzle holes depend also on needle lift) and of the injector closing time, thus strongly affecting the predicted volume of fuel injected per cycle.

The deformation of the injector body also affects the maximum control valve stroke, and a similar analysis can be performed to evaluate its effects on injector performance. Our study showed that this parameter does not play as important a role as the maximum needle stroke, because the effective flow area of the A hole is smaller than the one generated by the displacement of the control valve pin, and thus it is the A hole that controls the efflux from the control volume to the tank.

2.3.4 Masses, spring stiffness and damping factors

Components mass and springs stiffness k_j can be easily estimated. Whenever a spring is in contact to a moving element, the moving mass m_j value used in the model is the sum of the element mass and a third of the spring mass. In this way it is possible to correctly account for the effect of spring inertia too.

The evaluation of the damping factors β_j in Equation 31 is considerably more difficult. Considering the element moving in its liner, like needle and control piston, the damping factor takes into account the damping effects due to the oil that moves in the clearance and the friction between moving element and liner. The oil flow effect can be modelled as a combined Couette-Poiseuille flow (White, 1991) and the wall shear stress on the moving element surface can be theoretically evaluated. Experimental evidences show that friction effects are more relevant than the fluid-dynamics effects previously mentioned. Unfortunately, these can not be theoretically evaluated because their intensity is linked to manufacturing tolerances (both geometrical and dimensional). Therefore, damping factors must be estimated during the model tuning phase.



(a) Main injection: $ET_0=780\mu s$, $p_{r0}=135$ MPa

(b) Pilot injection: $ET_0=300\mu s$, $p_{r0}=80$ MPa

Fig. 14. Comparison between numerical and theoretical results

3. Model tuning and results

Any mathematical model requires to be validated by comparing its results with the experimental ones. During the validation phase some model parameters, which cannot be experimentally or theoretically evaluated, have to be carefully adjusted.

The model here presented was tested comparing numerical and experimental control valve lift x_c , control piston lift x_p , injected flow rate Q and injector inlet pressure p_{in} in several operating conditions. Figure 15 shows two of these validation tests and the good accordance between experimental and numerical results is evident.

Table 4 shows the value of the parameters that were adjusted during the tuning phase. These values can be used as starting points for the development of new injector models, but their exact value will have to be defined during model tuning for the reasons explained above.

After the tuning phase the model can be used to reproduce the injection system performance in its whole operation field. By way of example, Fig. 15 shows the experimental and numerical volume injected per stroke V_f and the percentage error of the numerical estimation.

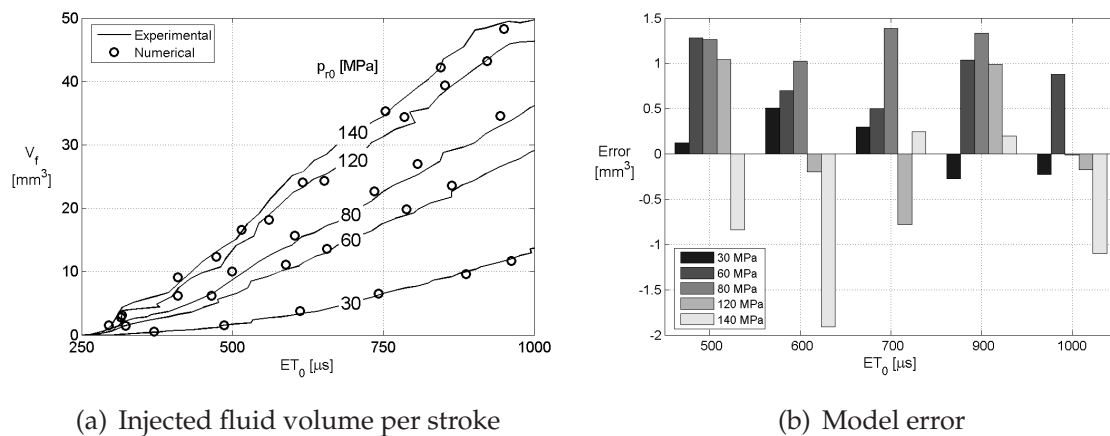


Fig. 15. Model validation

| Eq. 10 | | Eq. 12 | | Eq. 13 | Eq. 31 | | | | | |
|------------------|------------------|-------------------------------|------------------|------------------|-----------|-----------|-----------|-----------|-----------|--------|
| $\mu_h^d(\xi_0)$ | $\mu_h^d(\xi_M)$ | K_3 | K_4 | τ | β_n | β_N | β_P | β_c | β_a | [kg/s] |
| 0.75 | 0.85 | $0.28 \mu\text{m}/\text{MPa}$ | $63 \mu\text{m}$ | $25 \mu\text{s}$ | 6.1 | 6310 | 6.5 | 28 | 5.1 | |

Table 4. Tuning defined parameters

4. Nomenclature

| Symbol | Definition | Unit |
|----------------|---|-------------|
| A | Geometrical area | m^2 |
| C | Uniform pressure chamber | |
| c | Wave propagation speed | m/s |
| d | Hole Pipe diameter | m |
| e | Eccentricity | m |
| E | Young's modulus | Pa |
| ET | Injector solenoid energisation time | s |
| F | Force | N |
| f | Friction factor | |
| I | Electric current | A |
| K | Coefficient | |
| k | Spring stiffness | N/m |
| l | Length | m |
| m | Mass | kg |
| N | Number of coil turns | |
| p | Pressure | Pa |
| Q | Flow rate | m^3/s |
| r | Rail Fillet radius | m |
| R | Hydraulic resistance | |
| Re | Reynolds number | |
| S | Surface area | m^2 |
| t | Time | s |
| u | Average cross-sectional velocity of the fluid | m/s |
| V | Valve Volume | m^3 |
| W | Energy | J |
| X | Distance | m |
| x | Displacement Axial coordinate | m |
| β | Damping factor | kg/s |
| γ | switch (0=nozzle closed,1=nozzle open) | |
| Δ | Increment Drop | |
| Φ | Magnetic flux | Wb |
| ξ | Needle-seat relative displacement | m |
| μ | Contraction Discharge coefficient | |
| ρ | Density | kg/m^3 |
| τ | Wall shear stress Time constant | Pa s |
| \mathfrak{R} | Reluctance | H^{-1} |

| Subscript | Definition |
|-----------|-------------------------------|
| A | Control-volume discharge hole |
| a | Armature |
| B | Injector body |
| b | Seat |
| C | Compression |
| c | Control valve |
| D | Delivery |

| Symbol | Definition | Unit |
|--------------|-----------------------------------|------|
| d | Downstream | |
| E | Electromechanical | |
| e | Injection environment External | |
| f | Fuel | |
| h | Hole | |
| l | Inlet loss Liquid phase | |
| in | Injector inlet | |
| M | Maximum value | |
| m | Magnetic | |
| N | Nozzle | |
| n | Needle | |
| P | Piston | |
| R | Reaction Force | |
| r | Rail | |
| S | Sac | |
| s | Needle-seat | |
| T | Tank | |
| u | Upstream | |
| v | Vapour | |
| vc | Vena contracta | |
| Z | Control-volume feeding hole | |
| 0 | Reference value | |
| Superscripts | Definition | |
| d | Dynamic | |
| r | Relative | |
| s | Steady-state | |

5. References

- Amoia, V., Ficarella, A., Laforgia, D., De Matthaeis, S. & Genco, C. (1997). A theoretical code to simulate the behavior of an electro-injector for diesel engines and parametric analysis, *SAE Transactions* **970349**.
- Badami, M., Mallamo, F., Millo, F. & Rossi, E. E. (2002). Influence of multiple injection strategies on emissions, combustion noise and bsfc of a di common rail diesel engines, *SAE paper* **2002-01-0503**.
- Beatrice, C., Belardini, P., Bertoli, C., Del Giacomo, N. & Migliaccio, M. (2003). Downsizing of common rail d.i. engines: Influence of different injection strategies on combustion evolution, *SAE paper* **2003-01-1784**.
- Bianchi, G. M., Pelloni, P. & Corcione, E. (2000). Numerical analysis of passenger car hsd diesel engines with the 2nd generation of common rail injection systems: The effect of multiple injections on emissions, *SAE paper* **2001-01-1068**.
- Boehner, W. & Kumel, K. (1997). Common rail injection system for commercial diesel vehicles, *SAE Transactions* **970345**.
- Brusca, S., Giuffrida, A., Lanzafame, R. & Corcione, G. E. (2002). Theoretical and experimental analysis of diesel sprays behavior from multiple injections common rail systems, *SAE paper* **2002-01-2777**.

- Canakci, M. & Reitz, R. D. (2004). Effect of optimization criteria on direct-injection homogeneous charge compression ignition gasoline engine performance and emissions using fully automated experiments and microgenetic algorithms, *J. of Engineering for Gas Turbines and Power* **126**: 167–177.
- Catalano, L. A., Tondolo, V. A. & Dadone, A. (2002). Dynamic rise of pressure in the common-rail fuel injection system, *SAE paper* **2002-01-0210**.
- Catania, A., Dongiovanni, C., Mittica, A., Badami, M. & Lovisolo, F. (1994). Numerical analysis vs. experimental investigation of a distribution type diesel fuel injection system, *J. of Engineering for Gas Turbines and Power* **116**: 814–830.
- Catania, A. E., Dongiovanni, C., Mittica, A., Negri, C. & Spessa, E. (1997). Experimental evaluation of injector-nozzle-hole unsteady flow-coefficients in light duty diesel injection systems, *Proceedings of the Ninth Internal Pacific Conference on Automotive Engineering*, Bali, Indonesia.
- Chai, H. (1998). *Electromechanical Motion Devices*, Pearson Professional Education.
- Coppo, M. & Dongiovanni, C. (2007). Experimental validation of a common-rail injector model in the whole operation field, *J. of Engineering for Gas Turbines and Power* **129**(2): 596–608.
- Dongiovanni, C. (1997). Influence of oil thermodynamic properties on the simulation of a high pressure injection system by means of a refined second order accurate implicit algorithm, *ATA Automotive Engineering* pp. 530–541.
- Dongiovanni, C., Negri, C. & Roberto, R. (2003). A fluid model for simulation of diesel injection systems in cavitating and non-cavitating conditions, *Proceedings of the ASME ICED Spring Technical Conference*, Salzburg, Austria.
- Ficarella, A., Laforgia, D. & Landriscina, V. (1999). Evaluation of instability phenomena in a common rail injection system for high speed diesel engines, *SAE paper* **1999-01-0192**.
- Ganser, M. A. (2000). Common rail injectors for 2000 bar and beyond, *SAE paper* **2000-01-0706**.
- Henelin, N. A., Lai, M.-C., Singh, I. P., Zhong, L. & Han, J. (2002). Characteristics of a common rail diesel injection system under pilot and post injection modes, *SAE paper* **2002-010218**.
- Lefebvre, A. (1989). *Atomization and Sprays*, Hemisphere Publishing Company.
- Munson, B. R., Young, D. F. & Okiishi, T. H. (1990). *Fundamentals of Fluid Mechanics*, Wiley.
- Nasar, S. (1995). *Electric machines and power systems : Vol. 1. Electric Machines*, McGraw-Hill.
- Park, C., Kook, S. & Bae, C. (2004). Effects of multiple injections in a hsd diesel engine equipped with common rail injection system, *SAE paper* **2004-01-0127**.
- Payri, R., Climent, H., Salvador, F. J. & Favennec, A. G. (2004). Diesel injection system modelling. methodology and application for a first-generation common rail system, *Proceedings of the Institution of Mechanical Engineering* **Vol. 218 Part D**.
- Schmid, M., Leipertz, A. & Fettes, C. (2002). Influence of nozzle hole geometry, rail pressure and pre-injection on injection, vaporization and combustion in a single-cylinder transparent passenger car common rail engine, *SAE paper* **2002-01-2665**.
- Schommers, J., Duvinage, F., Stotz, M., Peters, A., Ellwanger, S., Koyanagi, K. & Gildein, H. (2000). Potential of common rail injection system passenger car di diesel engines, *SAE paper* **2000-01-0944**.
- Streeter, V. L., White, E. B. & Bedford, K. W. (1998). *Fluid Mechanics*, McGraw-Hill.
- Stumpp, G. & Ricco, M. (1996). Common rail - an attractive fuel injection system for passenger car di diesel engines, *SAE Transactions* **960870**.

- Von Kuensberg Sarre, C., Kong, S.-C. & Reitz, R. D. (1999). Modeling the effects of injector nozzle geometry on diesel sprays, *SAE paper* **1999-01-0912**.
- White, F. M. (1991). *Viscous Fluid Flow*, McGraw-Hill.
- Xu, M., Nishida, K. & Hiroyasu, H. (1992). A practical calculation method for injection pressure and spray penetration in diesel engines, *SAE Transactions* **920624**.
- Yamane, K. & Shimamoto, Y. (2002). Combustion and emission characteristics of direct-injection compression ignition engines by means of two-stage split and early fuel injection, *J. of Engineering for Gas Turbines and Power* **124**: 660–667.

IntechOpen

IntechOpen

IntechOpen

© 2010 The Author(s). Licensee IntechOpen. This chapter is distributed under the terms of the [Creative Commons Attribution-NonCommercial-ShareAlike-3.0 License](#), which permits use, distribution and reproduction for non-commercial purposes, provided the original is properly cited and derivative works building on this content are distributed under the same license.

IntechOpen

IntechOpen